Journal of Materials Chemistry A

ROYAL SOCIETY OF CHEMISTRY

PAPER

View Article Online
View Journal | View Issue

Cite this: J. Mater. Chem. A, 2022, 10, 3522

Intercalation of cobalt cations into Co_9S_8 interlayers for highly efficient and stable electrocatalytic hydrogen evolution†

Bin Tian,[a] Wojciech Kolodziejczyk,[a] Julia Saloni,[a] Pohlee Cheah,[a] Jing Qu,[a] Fengxiang Han,[a] Dongmei Cao,[b] Xianchun Zhu[a] and Yongfeng Zhao *[a]

Received 13th November 2021
Accepted 4th January 2022

DOI: 10.1039/d1ta09755e

rsc.li/materials-a

Non-noble metal based electrocatalysts for the hydrogen evolution reaction (HER) hold great potential for commercial applications. However, effective design strategies are greatly needed to manipulate the catalyst structures to achieve high activity and stability comparable to those of noble-metal based electrocatalysts. Herein, we present a facile route to synthesize layered Co_9S_8 intercalated with Co cations (Co^{2+}-Co_9S_8) (with interlayer distance up to 1.08 nm) *via* a one-step solvothermal method. Benefiting from a large interlayer distance and efficient electron transfer between layers, the Co^{2+}-Co_9S_8 hybrid shows outstanding electrocatalytic hydrogen evolution performance in an acid electrolyte. The electrocatalytic performance is even better than that of 20% Pt/C at the <−0.54 V region with an overpotential of 86 mV at a current density of 10 mA cm^{-2} in 0.5 mol L^{-1} H_2SO_4. More importantly, the system can maintain excellent stability for more than 12 h without obvious decay. This study not only presents a novel and efficient approach to synthesize cobalt sulfide intercalated with Co cations for stable electrocatalytic HER but also provides an avenue for the design of intercalated materials used in other energy applications.

Introduction

Since the first industrial revolution, the utilization of fossil fuels has brought great convenience to modern society but has also resulted in serious environmental problems.[1–3] Especially with the depletion of fossil fuels, it is urgent to construct a new energy system.[4] Solar energy is considered as an endless and green energy source. It will be an ideal energy system if we can convert solar energy into chemical fuels, which can then be stored and utilized. One of the promising strategies is the formation of hydrogen (H_2) through highly efficient and sustainable electrolysis of water owing to the abundant water sources on Earth.[5,6] So far, noble metal (Pt, Ir, Rh, *etc.*)-based materials have shown promising catalytic activities; however, scarce reserves and exorbitant prices limit their wide range of commercial applications.[7] The long-term stability of these precious metal catalysts is hardly satisfactory, especially in an acid electrolyte.[8]

In the past few decades, great efforts have been devoted to the development of non-noble metal-based catalysts for the hydrogen evolution reaction (HER). Particularly, earth-abundant transition metal chalcogenides (TMCs), such as MoS_2, Co_9S_8, FeS_2, *etc.*, have been demonstrated as promising catalytic materials for the HER inspired by the structure/composition of nitrogenase and hydrogenase.[9–12] But their activity is far from satisfactory compared with that of Pt-based catalysts due to low conductivity.[13] In addition, TMCs suffer from serious stability problems because of the dissolution or agglomeration during the reaction.[14] There have been reports that carbon materials, such as carbon nanotubes, graphene, and carbon dots, can accelerate the electron transfer to the active sites and stabilize the structure of catalysts.[15] Nevertheless, the performance reported to date is still unsatisfactory, partially due to the lack of efficient structure control for fully utilizing the active sites of the catalysts.

Recently, 2D materials, especially those with an ultrathin 2D structure, have attracted considerable attention because their excellent physical, chemical, electronic, and optical properties not only make them promising for technological applications but also provide opportunities to discover unexplored fundamental science.[16,17] The use of 2D material nanosheets as catalysts generally requires tedious exfoliation processes, which restricts mass production and industrial applications. In this regard, it is worth taking a new look at bulk materials, which have the potential to be excellent hosts for a large class of species (guests) within their inner planes. An intriguing idea is that the host and intercalant can operate synergistically to achieve high efficiency and stable catalytic performance. To date, most of the intercalation methods have involved ball milling of stoichiometric amounts of materials at high

[a]Department of Chemistry, Physics and Atmospheric Science, Jackson State University, Jackson, MS, 39217, USA. E-mail: yongfeng.zhao@jsums.edu

[b]Material Characterization Center, Louisiana State University, Baton Rouge, LA, 70803, USA

† Electronic supplementary information (ESI) available. See DOI: 10.1039/d1ta09755e

temperatures. The traditional approaches in chemical intercalation require electrochemical steps, limiting the concentration of the intercalant.[18]

Herein, we present a facile strategy to synthesize layered Co_9S_8 intercalated with Co^{2+} (Co^{2+}-Co_9S_8) *via* a one-step solvothermal method. Benefiting from a large interlayer distance and efficient electron transfer between layers, the Co^{2+}-Co_9S_8 hybrid shows outstanding electrocatalytic hydrogen evolution performance in an acid electrolyte. The catalytic performance is even better than that of 20% Pt/C at the <-0.54 V region, specifically with an overpotential of 86 mV at 10 mA cm^{-2} in 0.5 mol L^{-1} H_2SO_4. More importantly, no carbon materials were used in our system, and the intercalation of Co cations significantly enhanced the stability of Co_9S_8. This study not only presents a novel and efficient approach to synthesize cobalt sulfide intercalated with Co cations for the electrocatalytic HER but also provides a new avenue for the design of intercalated materials used in other energy applications.

Experimental

Chemicals and reagents

Cobalt nitrate hexahydrate ($Co(NO_3)_2 \cdot 6H_2O$, Sigma-Aldrich, ACS reagent, ≥98%), phosphorus pentasulfide (P_4S_{10}, Sigma-Aldrich, ACS reagent, 99%), anhydrous ethanediamine ($C_2H_8N_2$, Fisher Scientific, ACS reagent, 99.9%), absolute ethanol (C_2H_5OH, Fisher Scientific, ACS reagent, ≥99%), concentrated sulfuric acid (H_2SO_4, Fisher Scientific, ACS reagent, ≥98%), and Nafion solution (Sigma-Aldrich, 5%) were used directly without any further purification. The deionized water used throughout all the experiments was purified using a Millipore system.

Synthesis of Co^{2+}-Co_9S_8

Certain amounts of cobalt nitrate (1.72 mmol, $Co(NO_3)_2 \cdot 6H_2O$) and phosphorus pentasulfide (0.5 mmol, P_4S_{10}) were dissolved in 70 mL ethanediamine (EDA) to form a grey solution. After stirring at room temperature for 0.5 h, the mixed solution was transferred into a 100 mL Teflon-lined autoclave, and then reacted at 140 °C for 24 h. After the mixture was cooled down to room temperature, a black product (named Co^{2+}-Co_9S_8) was obtained. The product was washed with deionized water and ethanol, and then dried in an oven at 50 °C for 12 h. The amount of Co^{2+} intercalated into layered Co_9S_8 was controlled by adjusting the ratio of starting materials.

Synthesis of Co_9S_8

The synthesis of pristine Co_9S_8 was performed following a method reported in the literature.[19] In a typical synthesis, cobalt(II) acetate tetrahydrate (5 mmol) and thiourea (5 mmol) were dissolved in ethylene glycol (30 mL) under vigorous stirring for 30 min. The resulting solution was transferred into an autoclave, and the autoclave was then sealed and maintained at 200 °C for 48 h. When the autoclave was cooled down to room temperature, the samples were washed with distilled water several times to obtain the pristine Co_9S_8 catalyst.

Synthesis of CoS_2

The synthesis of CoS_2 catalysts was achieved by a previously reported method.[20] Typically, $CoCl_2 \cdot 6H_2O$ (2.5 mmol) and $Na_2S_2O_3 \cdot 5H_2O$ (2.5 mmol) were dissolved in 60 mL ultrapure water under magnetic stirring conditions. Then the mixed solution was transferred into a 100 mL Teflon-lined stainless steel autoclave and subsequently agitated for another 2 h. The sealed mixture then reacted at 150 °C for 12 h. After the reaction, the autoclave was cooled down to room temperature. The black product was harvested by filtration and washed with CS_2, ethanol, and deionized water, respectively, before drying at 80 °C overnight.

Synthesis of $Co(OH)_2$

The synthesis of cobalt hydroxide ($Co(OH)_2$) was reported in a previous study.[21] In detail, 4.0 mmol $CoCl_2$ (anhydrous) and 2 mmol urea were firstly dispersed in 80 mL pure water. After stirring for 2 h at room temperature, the mixture was transferred into a 100 mL Teflon-lined stainless steel autoclave, and subsequently reacted at 150 °C for 12 h. After the reaction, the autoclave was cooled to room temperature. The black product was harvested by filtration and washed with ethanol and deionized water before drying at 80 °C overnight.

Electrochemical measurements

All the electrochemical measurements were carried out on an SP-150 electrochemical workstation (EC-Lab, Germany) with a standard three-electrode setup (in which a saturated calomel electrode (SCE) served as the reference electrode and a 1 cm^2 platinum plate served as the counter electrode, respectively, and the as-synthesized samples served as the working electrode). A carbon cloth (CC, 0.1 cm^2) was used as the support for the working electrode. In detail, 4.5 mg of the samples and 20 μL Nafion solution (5 wt%) were dispersed in 1.5 mL pure water and 100 μL ethanol, and then sonicated for 30 min to form a solution. Then, 20 μL of the ink was loaded onto the surface of the CC and dried at room temperature to obtain the working electrode (~0.56 mg cm^{-2}). The HER performances were evaluated in Ar-saturated 0.5 mol L^{-1} H_2SO_4. The electrocatalytic activity of the samples was examined by obtaining polarization curves using linear sweep voltammetry (LSV) with a scan rate of 10 mV s^{-1} at room temperature. Electrochemical impedance spectroscopy (EIS) measurements were performed at different potentials from 10^5 to 10^{-2} Hz. EIS data were analyzed and fitted with ZSimpWin software. The stability measurements were performed by cyclic voltammetry scanning for 2000 cycles (CV, sweep rate, 100 mV s^{-1}) and long-term chronoamperometry. Note that the values of current density were all normalized with the geometric surface area and corrected by the background currents. All tested values in our experiments were converted to the reversible hydrogen electrode (RHE) scale using eqn (1)

$$E_{RHE} = E_{SCE} + 0.059\ pH + E^0_{SCE}\ (E^0_{SCE} = 0.242\ V) \quad (1)$$

Characterization

The X-ray diffraction (XRD) patterns were collected on a Rigaku X-ray diffractometer using Cu Kα radiation ($\lambda = 0.154$ nm) at a 2θ scan rate of 0.5° s^{-1}. The accelerating voltage and applied current adopted were 40 kV and 80 mA, respectively. High-resolution transmission electron microscopy (HRTEM) and transmission electron microscopy (TEM) analyses were conducted on a Tecnai G2 F20 transmission electron microscope with a 200 kV accelerating voltage. Scanning electron microscopy (SEM) images were acquired on a TESCAN LYRA3 at an accelerating voltage of 5.0 or 10 kV. Energy Dispersive X-ray Spectroscopy (EDS) microanalysis was performed on a Noran System 7 from Thermo Scientific using an acceleration voltage of 20 kV. X-ray photoelectron spectroscopy (XPS) measurements were performed on an ESCALAB 250Xi electron spectrometer with a Mg Kα (1253.6 eV) source. All binding energies were referenced to the C 1s peak at 284.8 eV from adventitious carbon. The content of Co element in the as-prepared samples was analyzed using an inductively coupled plasma-atomic emission spectrometer (ICP-AES) on a PerkinElmer Optima 7300DV. Fourier transform infrared (FT-IR) spectra ranging from 4000 to 400 cm^{-1} were recorded by averaging 32 scans with a resolution of 4 cm^{-1} on a Thermo Nicolet 6700 FT-IR spectrometer equipped with a mercury cadmium telluride detector. The thickness of catalysts was examined on an atomic force microscope (AFM, Dimension 3100).

Theoretical calculation

In this work, all calculations were conducted with a Quantum Espresso Package module based on density functional theory (DFT) methods.[22–24] The form of the Perdew–Burke–Ernzerhof, PBE, functional at the generalized gradient approximation, GGA, level was employed as the exchange–correlation functional.[25–27] A plane wave basis set was used to describe electron wave functions with a cut-off energy of 550 eV. The irreducible Brillouin zone was sampled by Monkhorst–Pack *k* point meshes of $2 \times 2 \times 1$ during geometry optimization and electronic properties calculations.[28] The lattice parameters and the positions of atoms were relaxed until the maximum force, the maximum stress, the maximum displacement, maximal energy change and the self-consistent field tolerance were less than 1×10^{-8} eV per atom. The monolayer of the Co_9S_8 crystal was constructed by cutting the bulk crystal structure along the (002) plane. A cell consisting of nine cobalt atoms and eight sulfur atoms was used as a slab model in this study. Additionally, the vacuum space was created with the set parameter of 10.8 Å along the *Z* direction to manifest the experimental conditions. Next, the slab model of the monolayer Co_9S_8 was optimized, and the following parameters have been obtained: $a = 9.927$ Å, $b = 9.927$ Å, $c = 10.800$ Å, $\alpha = \beta = \gamma = 90^\circ$. Based on the slab model computational results, the Gibbs free energy, ΔG, has been calculated applying the formula $\Delta G = \Delta E + 0.24$ eV as proposed by Peng *et al.*[29] ΔE of the reaction was calculated as $E_{\text{complex-H2}} - E_{\text{complex-HH}}$. For the complex with Co^{2+}, the binding energy of the Co^{2+}-H_2 complex has been subtracted from the final ΔE to consider two independent molecules instead of the Co^{2+}-H_2 complex.

$$\Delta G = (\Delta E_{\text{complex-H2}} - \Delta E_{\text{complex-HH}} - \Delta E_{\text{bindingH2}}) + 0.24 \quad (2)$$

Results and discussion

Synthesis and characterization of Co^{2+}-Co_9S_8

The Co^{2+}-Co_9S_8 catalysts have been prepared by a one-step solvothermal method that used cobalt nitrate and phosphorus pentasulfide as starting materials and EDA as solvent (see the Experimental section for the detailed process). The schematic illustration of the synthesis is shown in Fig. 1a. The as-prepared products have been first characterized by X-ray diffraction (XRD) (Fig. 1b). For comparison, the XRD analysis of CoS_2, pristine Co_9S_8, and $Co(OH)_2$ has been also carried out. In the pristine Co_9S_8 pattern of Fig. 1b, the peaks at 15.5°, 17.8°, 29.8°, 39.7°, 47.9°, and 52.2° can be identified as the (111), (200), (311), (331), (511) and (440) planes of the cubic Co_9S_8 phase (PDF#86-2273), respectively.[19] However, in Co cations intercalated Co_9S_8 samples, we only observe the characteristic peaks of the (111), (200), (311), and (331) facets as indicated by black dots. The high index diffraction peaks of (511) and (440) disappear. Furthermore, the crystallinity of Co_9S_8 after being intercalated with Co cations shows an obvious decrease compared to that of pristine Co_9S_8 (Fig. S1†). All these results can be attributed to some disorder within its *ab* plane owing to the intercalation of Co cations.[30,31]

As solid evidence, two new peaks are observed at low angles (8.18° and 16.36°) of XRD for the Co^{2+}-Co_9S_8 samples, suggesting a long-range order layered structure of Co^{2+}-Co_9S_8. The interlayer distance of Co^{2+}-Co_9S_8 is further calculated based on the Bragg equation. The result suggests that the as-obtained Co^{2+}-Co_9S_8 samples show an expanded interlayer distance of 1.08 nm. The layered structure is directly observed from the HRTEM, and the interlayer distance is in accordance with the interlayer spacing measured in the edge area of HRTEM (Fig. S2a†). In addition, the obvious shift of the (311) peaks after the intercalation of Co cations suggests that the intercalated Co cations have an interaction with Co_9S_8 layers.[32]

In order to observe the layered structure of Co^{2+}-Co_9S_8, the transmission electron microscopy (TEM) and scanning electron microscopy (SEM) of the samples have been carried out. As presented in Fig. 1c, the typical TEM image exhibits a layered structure with a size of ~600 nm. A closer inspection of Co^{2+}-Co_9S_8 shows a lattice spacing of 0.299 nm, which can be assigned to the (311) plane of Co_9S_8 (Fig. 1d), indicating poor crystallinity which is consistent with the result of XRD.[33] This is consistent with the result of TEM selected area electron diffraction (Fig. S3†). From the cross-section of the Co^{2+}-Co_9S_8 samples, an obvious layered structure is presented (Fig. S4a.†)

To illustrate the elemental composition and distribution in the Co^{2+}-Co_9S_8 samples, SEM elemental mapping has been performed. As shown in Fig. 1e, the two main elements of Co and S are observed in the Co^{2+}-Co_9S_8 samples, and no phosphorus (P) elemental signal is detected. As we expected, the

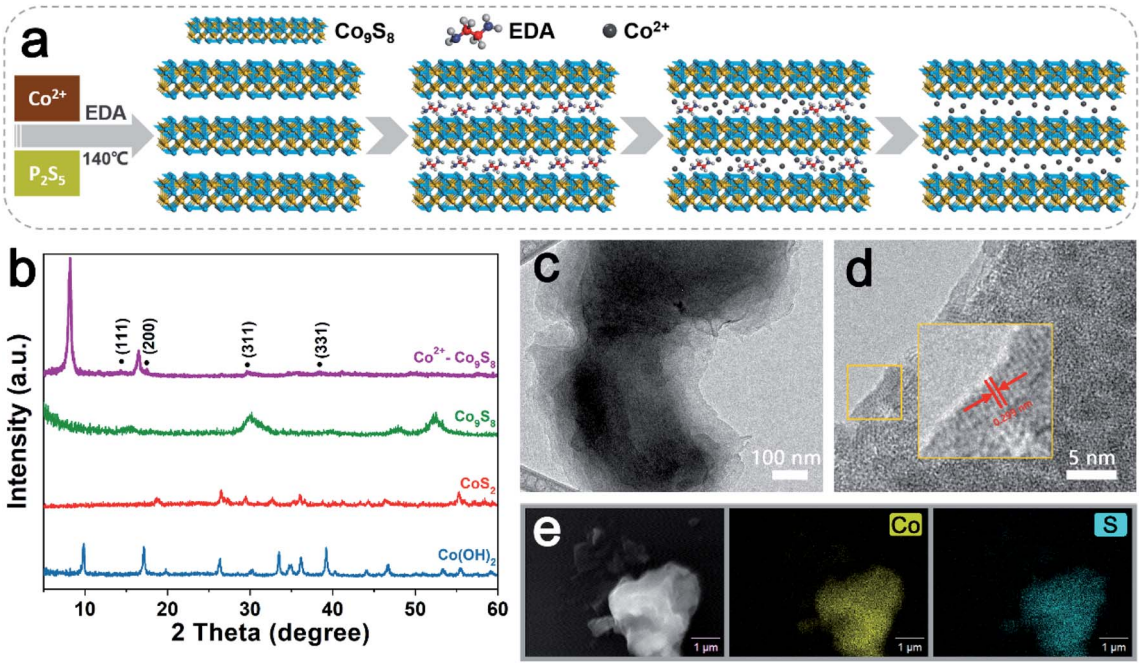

Fig. 1 (a) Schematic illustration for the synthesis of Co_9S_8 intercalated with Co^{2+}. (b) XRD patterns of $Co(OH)_2$, CoS_2, pristine Co_9S_8, and Co cations intercalated into Co_9S_8. The black dots indicate diffraction peaks corresponding to the Co_9S_8 phase. (c) TEM and (d) HRTEM images of Co^{2+}-Co_9S_8. (e) SEM EDS elemental mapping of Co^{2+}-Co_9S_8.

amount of Co element is higher than that of S elements in the Co^{2+}-Co_9S_8 samples based on SEM elemental analysis (Fig. S4b and c†). More importantly, the Co and S elements disperse evenly throughout the samples, and the distribution of S and Co elements overlaps. Fourier transform infrared (FT-IR) (Fig. S5†) results show the same peak center at 1045 cm^{-1} in the Co^{2+}-Co_9S_8, CoS_2, and Co_9S_8 curves, which can be attributed to the vibration of the Co–S bond. Furthermore, we have obtained the Raman spectrum of the prepared Co^{2+}-Co_9S_8. As shown in Fig. S6,† the spectrum of the Co^{2+}-Co_9S_8 sample shows the typical Raman peaks of Co_9S_8, which further confirm the formation of the Co_9S_8 phase in the Co^{2+}-Co_9S_8 sample.[34] Furthermore, the Raman spectra of Co^{2+}-Co_9S_8 in the range of 100–2500 cm^{-1} show no obvious peaks, which indicates that carbonization of EDA did not occur in the solvothermal process. In combination with XRD, we can conclude that these superfluous Co cations are intercalated into layered Co_9S_8, and resulted in structural disorder within its *ab* plane, and poor crystallinity, subsequently. Moreover, atomic force microscopy (AFM) has been performed to detect the thickness of the as-obtained Co^{2+}-Co_9S_8 samples. As shown in Fig. S7,† the thickness of the layered Co_9S_8 is ~73.0 nm, which is about 68 layers based on the interlayer distance and the thickness of a single layer.[35]

X-ray photoelectron spectroscopy (XPS) has been then carried out to identify the elemental chemical state in the Co^{2+}-Co_9S_8 samples. As a control, the chemical state of pristine Co_9S_8 is also studied using C 1s (284.8 eV) as the reference. The XPS survey spectrum (Fig. S8†) shows the main existence of Co and S elements and the absence of an obvious peak of P 2p spectra (Fig. S9†), which is consistent with the SEM elemental map study. The high-resolution XPS spectrum of Co 2p in Co_9S_8 samples (Fig. 2a) shows three peaks for Co $2p_{3/2}$ (777.7, 780.6, and 785.6 eV), and the Co $2p_{1/2}$ peak is also deconvoluted into

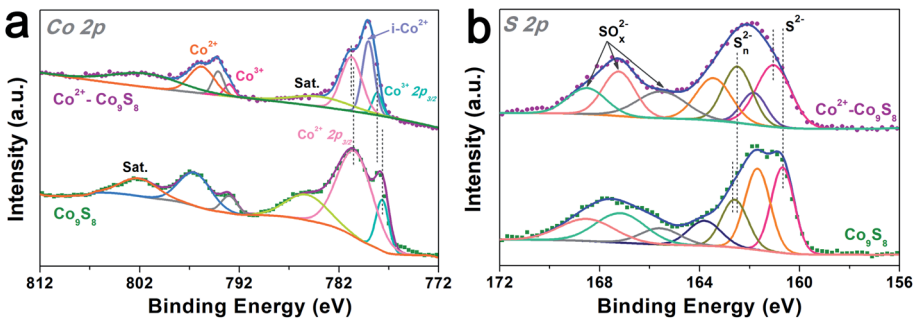

Fig. 2 The high-resolution XPS spectra of (a) Co 2p and (b) S 2p in pristine Co_9S_8 and Co^{2+}-Co_9S_8 samples.

three components with binding energies at 793.0, 796.7, and 802.1 eV. The peaks of 777.7 and 793.0 eV can be attributed to the $2p_{3/2}$ and $2p_{1/2}$ core levels of Co^{3+}, while the peaks centered at 780.6 and 796.7 eV are assigned to the $2p_{3/2}$ and $2p_{1/2}$ core levels of Co^{2+}, respectively. The peaks at 785.6 and 802.1 eV are the shake-up satellite peaks of Co elements.[19] As we expected, in addition to Co^{2+} and Co^{3+} of Co_9S_8, we also detect a binding energy centered at 779.1 eV for Co 2p in the high-resolution spectrum of Co^{2+}-Co_9S_8. This binding energy can be attributed to intercalated Co^{2+} (i-Co^{2+}).[36,37] Combining the XRD and SEM results, we conclude that some Co cations are successfully intercalated into and have an interaction with Co_9S_8 interlayers.

Fig. 2b shows the high-resolution spectra of S 2p for Co_9S_8 and Co^{2+}-Co_9S_8 catalysts. In pristine Co_9S_8, the binding energy at 160.7 and 162.7 eV can be attributed to the S $2p_{3/2}$ of S^{2-} and S_n^{2-} in Co_9S_8.[38] The peaks of 161.7 and 163.9 eV are assigned to the corresponding $2p_{1/2}$ core levels of S 2p. The binding energies centered at 165.6, 167.3 and 168.5 eV are due to the oxidation state of S. In the spectrum of Co^{2+}-Co_9S_8, the same chemical states of S^{2-} and S_n^{2-} are detected, confirming the formation of Co_9S_8 in Co^{2+}-Co_9S_8. The binding energy shifts are also observed in the Co 2p and S 2p spectra in the Co^{2+}-Co_9S_8 catalysts. In particular, after the intercalation of Co(II) ions into Co_9S_8, the Co element manifests higher binding energy and the S element exhibits lower binding energy. These shifts can be caused by the interaction between intercalated Co(II) ions and Co_9S_8 layers, thus resulting in charge redistribution in Co_9S_8 layers.[39]

Based on the above analysis, we propose a reasonable formation process of Co_9S_8 intercalated with Co cations as illustrated in Fig. 1a. Bulk Co_9S_8 is firstly formed under mild conditions when using cobalt nitrate and phosphorus pentasulfide as starting materials in EDA. In general, it is difficult for metal ions to enter into interlayers due to the strong van der Waals forces between layers; however, it has been reported that some mechanical methods and organic solvents can effectively overcome van der Waals forces to achieve the purpose of exfoliation.[40,41] In particular, EDA is an effective organic solvent to open layers of g-C_3N_4 at high temperatures and pressures.[42] In our system, we reason that EDA plays a similar role in enlarging the Co_9S_8 interlayer distance. The organic solvent of EDA first enters into interlayers of Co_9S_8 at high temperatures and pressures and expands the interlayer distance of Co_9S_8. Then, through the interaction of Coulomb forces, some cobalt ions enter into interlayers and react with layers through a surface charge to form Co_9S_8 intermediate species intercalated with Co cations and EDA. After water washing, the EDA in the interlayer is swilled out, and stable Co cations intercalated into Co_9S_8 samples are formed.

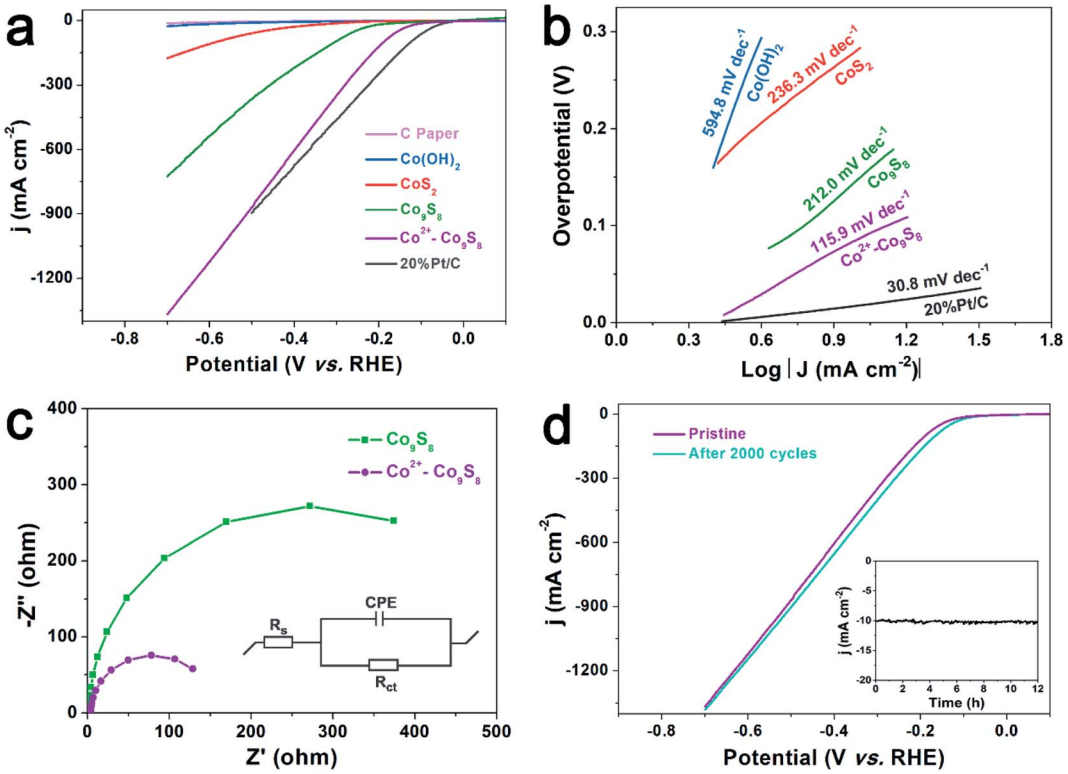

Fig. 3 The electrochemical hydrogen evolution performance in 0.5 mol L^{-1} H_2SO_4 electrolyte. (a) The polarization curves of $Co(OH)_2$, CoS_2, pristine Co_9S_8, and Co^{2+}-Co_9S_8 catalysts (as well as 20% Pt/C and C paper for comparison); the scan rate is 10 mV s^{-1}. (b) The Tafel plots of $Co(OH)_2$, CoS_2, pristine Co_9S_8, Co^{2+}-Co_9S_8, and 20% Pt/C. (c) The Nyquist plots of pristine Co_9S_8 and Co^{2+}-Co_9S_8 samples. (d) Polarization curves of the Co^{2+}-Co_9S_8 catalyst at a scan rate of 10 mV s^{-1} after CV cycling for the stability test. The inset is potentiostatic electrolysis of Co^{2+}-Co_9S_8 for 12 h (the potential we applied is −97 mV *vs.* RHE). Note that the values of current density are all normalized with the geometric surface area and corrected by the background currents.

Electrocatalytic performance of Co^{2+}-Co_9S_8

To evaluate the electrocatalytic HER activity of the as-synthesized catalysts, a standard three-electrode electrochemical apparatus is constructed by using 0.5 mol L^{-1} H_2SO_4 as an electrolyte. Bare CC and 20% Pt/C are also tested as the reference under identical conditions. As shown in the linear sweep voltammetry (LSV) curves (Fig. 3a), the Co^{2+}-Co_9S_8 hybrid requires an overpotential of 86 mV to achieve a current density of 10 mA cm^{-2}, which prominently outperforms $Co(OH)_2$ (501 mV), CoS_2 (281 mV), and Co_9S_8 (148 mV). The value is closer to an overpotential of 41 mV for 20% Pt/C. This result suggests that the intercalated Co cations play a significant role in enhancing the HER activity of Co_9S_8. Moreover, the anodic current density of the Co^{2+}-Co_9S_8 composite surpasses that of 20% Pt/C when the applied overpotential exceeds −540 mV, highlighting the advantage of the fabricated hybrid electrode in facilitating a faster hydrogen evolution rate for large-scale applications. By plotting the overpotential (η) against log current ($\log j$), the kinetic parameters of the HER have been calculated. The linear part of the Tafel plots (Fig. 3b) reveals Tafel slopes of ~594.8, ~263.2, ~212.0, and ~30.8 mV dec^{-1} for $Co(OH)_2$, CoS_2, Co_9S_8, and 20% Pt/C, respectively. In contrast, Co^{2+}-Co_9S_8 gives a smaller Tafel slope of 115.9 mV dec^{-1} than that of pristine Co_9S_8 and even smaller than that of the reported advanced systems (Table S1†), demonstrating faster HER kinetics after intercalation with Co cations. The HER process likely undergoes the Volmer–Heyrovsky mechanism on the Co^{2+}-Co_9S_8 hybrid, which accelerates the water dissociation and hydrogen adsorption rates, thereby leading to an enhanced HER activity.[43]

To explore the charge-transfer properties and the role of intercalated Co cations during the HER process, electrochemical impedance spectroscopy (EIS) experiments have been undertaken. The semidiameter value of the Co^{2+}-Co_9S_8 system is much smaller than that of pristine Co_9S_8 (Fig. 3c), implying that a smaller electron transfer resistance is achieved for Co^{2+}-Co_9S_8. Furthermore, we give the corresponding relevant equivalent circuits. As shown in Fig. 3c, the inset shows the equivalent circuit model used to fit the experimental data. It can be seen that all the plots exhibit a quasi-semicircle in the high-frequency region. The charge-transfer resistances R_{ct} of the Co^{2+}-Co_9S_8 and pristine Co_9S_8 electrodes are 151 and 543 Ω, respectively. The lower resistance of the Co^{2+}-Co_9S_8 electrode may be attributed to the effective electron transfer between Co_9S_8 layers. This further confirms that the intercalated Co cations can effectively promote the electron transfer between Co_9S_8 layers.[44] In addition, we synthesize different Co^{2+}-Co_9S_8 samples with intercalation of different amounts of Co cations. As shown in Fig. S10a,† the interlayer distance of Co_9S_8 increases with the intercalated Co amount increasing from 1.05 to 1.08 and then 1.10 nm. Furthermore, we have tested the electrocatalytic HER activity in acid solution of different Co_9S_8 samples with different layer spacing. Fig. S10b† shows that the HER activity first increases and then decreases with increasing interlayer distance. This phenomenon can be attributed to the following reason. First, when the interlayer distance is smaller than 1.08 nm, there are abundant active sites and more effective charge transfer between the Co_9S_8 interlayers, thus leading to higher HER activity. However, further increasing the interlayer distance of Co_9S_8 would cause poor charge transfer between layers although it still maintains abundant active sites, and thus lead to the decrease of HER activity.[45,46]

In addition to high activity, long-term catalytic durability is also very critical in practical applications. After sweeping for 2000 CV cycles between 1.3 and −0.7 V (*vs.* RHE) at 100 mV s^{-1}, the Co^{2+}-Co_9S_8 electrode almost fully retains its original activity (Fig. 3d), proving the salient catalytic stability. The stability is also indicated by the chronoamperometric response that displays an imperceptible decay in the overpotential at 10 mA cm^{-2} after a continuous polarization period of 12 h (inset in Fig. 3d). To further confirm the stability of the prepared Co^{2+}-Co_9S_8 catalysts for the electrocatalytic HER, the Raman and XPS spectra of Co^{2+}-Co_9S_8 after reaction have been recorded. As shown in Fig. S11,† the Raman spectrum of the Co^{2+}-Co_9S_8 sample after a 12 h reaction shows an unobvious change; however, the peak center at 667 cm^{-1} shows a slight shift, which may be attributed to the change of layer spacing. This may arise from the loss of intercalated Co^{2+}. Furthermore, Fig. S12† shows the high-resolution spectra of Co 2p and S 2p. Compared to that of the sample before reaction, the XPS spectrum does not show an obvious change after reaction, which further suggests the excellent stability of the prepared Co^{2+}-Co_9S_8 sample.

Mechanism study

Inspired by the remarkable HER performance, including activity and stability, of the synthesized Co^{2+}-Co_9S_8 catalysts, we further study the intrinsic mechanism of improving the HER *via* intercalation of Co cations. The first is high HER activity. On the one hand, as mentioned above, effective electron transfer between Co_9S_8 layers is beneficial to improve HER activity. On the other hand, after intercalating Co cations between layers, the larger interlayer distance leads to exposing more active sites similar to single-layer materials, and thus higher HER activity.[47] To support our hypothesis, we have tested the BET surface area and calculated the electrochemical surface active on the surface of the samples according to nitrogen adsorption–desorption isotherms and CV curves.[48] As shown in Table S2 and Fig. S13,† the Co^{2+}-Co_9S_8 catalyst shows an electrically active surface area of 671 mF cm^{-2}, which is much higher than that of the pristine Co_9S_8 catalyst (158 mF cm^{-2}). However, the Co^{2+}-Co_9S_8 system (43.4 m^2 g^{-1}) exhibits a smaller BET surface area and larger pore volume than those of the pristine Co_9S_8 system (55.4 m^2 g^{-1}). This result provides solid evidence for higher HER activity in the Co^{2+}-Co_9S_8 system upon intercalation of Co cations. In addition, after the intercalation of Co cations into Co_9S_8 layers, the electronic configurations and related interfacial properties of Co_9S_8 will also change and thus affect the adsorption and desorption of the hydrogen atom.[49] As shown in Table S3,† after intercalation of Co cations into the Co_9S_8 interlayer, the value of hydrogen adsorption free energy (ΔE_H) shows an obvious decrease, which is beneficial to the desorption of formed H_2. Furthermore, to gain further insight into the underlying mechanism of the HER catalysis, density functional theory

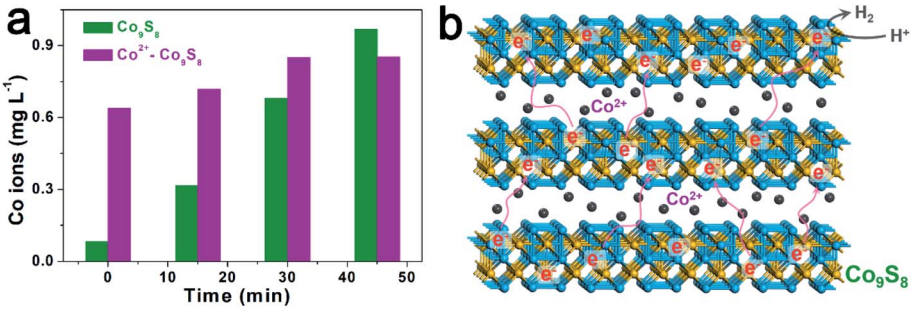

Fig. 4 The concentration of Co cations in electrolyte with the electrocatalytic reaction extending from 0 to 45 min in pristine Co_9S_8 and the Co cations intercalated Co_9S_8 system. (b) Schematic illustration of the electrocatalytic hydrogen evolution reaction process on Co cations intercalated Co_9S_8 catalysts.

(DFT) calculations have been performed for the Gibbs free energy for hydrogen adsorption of catalysts. The adsorption Gibbs free energy of H* (ΔG_{H^*}) on the catalysts serves as a parameter for the evaluation of HER activity. A large and negative value of ΔG_{H^*} indicates strong chemical adsorption, while a large and positive ΔG_{H^*} represents weak H* adsorption.[33] A catalyst that yields an absolute value of $\Delta G_{H^*} \approx 0$ is considered a good candidate for the HER, whether it is positive or negative. To further investigate the active centers, the free energy ΔG_{H^*} on Co^{2+}-Co_9S_8 and pristine Co_9S_8 systems was calculated. As shown in the Gibbs free-energy diagram of Fig. S14,† the calculations indicate that the absolute value of ΔG_{H^*} for Co^{2+}-Co_9S_8 is smaller than that of pristine Co_9S_8, and the favorable H* adsorption kinetics of the Co^{2+}-Co_9S_8 system is better than that of the pristine Co_9S_8. This is in good agreement with the electrochemical test results.

The second is high HER stability. A previous study suggests that the high HER activity of cobalt sulfide originates from the active sites formed on defects after dissociation of Co cations, which would lead to low stability.[50] In this regard, we propose that the intercalated Co cations can effectively inhibit the dissociation of Co cations in Co_9S_8 and thus lead to excellent HER stability. To confirm this speculation, we have detected the amount of Co cations in the electrolyte with increasing reaction time. As shown in Fig. 4a, in the pristine Co_9S_8 system, the amount of Co cations in the electrolyte shows a continuous increase with the reaction time from 0 to 45 min; however, in the Co^{2+}-Co_9S_8 system, the amount of Co cations in the electrolyte shows a trend of first increasing and then staying constant. This result can be attributed to the dissociation of partially intercalated Co cations instead of Co cations in the lattice, which leads to a dynamic equilibrium of Co cations between the electrolyte and the Co^{2+}-Co_9S_8 electrode. As a result, excellent HER stability is achieved for the Co^{2+}-Co_9S_8 system.

Based on the above experiments and analysis, we propose a tentative mechanism of improving electrocatalytic HER performance *via* the Co^{2+}-Co_9S_8 catalyst (as shown in Fig. 4b). The high HER activity is mainly due to two factors: (1) more active sites caused by a large interlayer distance, and (2) effective electron transfer between layers due to intercalated Co cations. The high HER stability mainly originates from the effective inhibition of the dissociation of Co cations in Co_9S_8.

Conclusions

In summary, we have demonstrated that the one-step solvent method is an efficient method to synthesize layered Co_9S_8 intercalated with Co cations, and it shows significant superiority in the electrocatalytic HER. The as-prepared Co^{2+}-Co_9S_8 electrode exhibits outstanding performance, including low overpotentials and faster kinetics for the HER as well as remarkable long-term catalytic durability. In particular, it shows a better HER activity than 20% Pt/C at the <-0.54 V region owing to the expanded interlayer distance and efficient electron transfer between layers. Furthermore, this system shows excellent stability for more than 12 h without obvious decay because the intercalation of Co cations can effectively inhibit the dissociation of Co cations from Co_9S_8. This study not only presents a novel and efficient approach to synthesize cobalt sulfide intercalated with Co cations for stable electrocatalytic HER but also provides an avenue for the design of intercalated materials used in other energy applications.

Conflicts of interest

There are no conflicts to declare.

Acknowledgements

This research was supported by the National Science Foundation (grant numbers: HRD-1700390, DMR-2000135) and the NSF EPSCoR (grant number: OIA-1757220). We thank Dr Losovyj for assistance with XPS experiments, Dr Islam for electrochemical analysis, and Dr Pradhan for AFM measurements.

References

1 B. You and Y. Sun, *Acc. Chem. Res.*, 2018, **51**, 1571–1580.
2 I. Roger, M. A. Shipman and M. D. Symes, *Nat. Rev. Chem.*, 2017, **1**, 0003.
3 Q. Lei, R. Chen, Y. Zhao, H. Chen, X. Long, J. Tan and X. Wang, *ChemSusChem*, 2020, **13**, 3605–3613.

4 Y. Wang, B. Kong, D. Zhao, H. Wang and C. Selomulya, *Nano Today*, 2017, **15**, 26–55.
5 J. Wang, W. Cui, Q. Liu, Z. Xing, A. M. Asiri and X. Sun, *Adv. Mater.*, 2016, **28**, 215–230.
6 J. Qi, W. Zhang and R. Cao, *Adv. Energy Mater.*, 2018, **8**, 1701620.
7 B. Xiong, L. Chen and J. Shi, *ACS Catal.*, 2018, **8**, 3688–3707.
8 Z. Chen, K. Leng, X. Zhao, S. Malkhandi, W. Tang, B. Tian, L. Dong, L. Zheng, M. Lin, B. S. Yeo and K. P. Loh, *Nat. Commun.*, 2017, **8**, 14548.
9 Z. Wu, J. Wang, K. Xia, W. Lei, X. Liu and D. Wang, *J. Mater. Chem. A*, 2018, **6**, 616–622.
10 S. Dou, L. Tao, J. Huo, S. Wang and L. Dai, *Energy Environ. Sci.*, 2016, **9**, 1320–1326.
11 X. Zou, Y. Wu, Y. Liu, D. Liu, W. Li, L. Gu, H. Liu, P. Wang, L. Sun and Y. Zhang, *Chem*, 2018, **4**, 1139–1152.
12 X. Du, J. Huang, J. Zhang, Y. Yan, C. Wu, Y. Hu, C. Yan, T. Lei, W. Chen, C. Fan and J. Xiong, *Angew. Chem., Int. Ed.*, 2019, **58**, 4484–4502.
13 Q. Lu, Y. Yu, Q. Ma, B. Chen and H. Zhang, *Adv. Mater.*, 2016, **28**, 1917–1933.
14 L. Wang, X. Wu, S. Guo, M. Han, Y. Zhou, Y. Sun, H. Huang, Y. Liu and Z. Kang, *J. Mater. Chem. A*, 2017, **5**, 2717–2723.
15 J. Yin, J. Jin, H. Lin, Z. Yin, J. Li, M. Lu, L. Guo, P. Xi, Y. Tang and C.-H. Yan, *Adv. Sci.*, 2020, **7**, 1903070.
16 Y. Liu, C. Xiao, P. Huang, M. Cheng and Y. Xie, *Chem*, 2018, **4**, 1263–1283.
17 K. C. Kwon, J. M. Suh, R. S. Varma, M. Shokouhimehr and H. W. Jang, *Small Methods*, 2019, **3**, 1800492.
18 K. J. Koski, C. D. Wessells, B. W. Reed, J. J. Cha, D. Kong and Y. Cui, *J. Am. Chem. Soc.*, 2012, **134**, 13773–13779.
19 L.-L. Feng, M. Fan, Y. Wu, Y. Liu, G.-D. Li, H. Chen, W. Chen, D. Wang and X. Zou, *J. Mater. Chem. A*, 2016, **4**, 6860–6867.
20 X. H. Chen and R. Fan, *Chem. Mater.*, 2001, **13**, 802–805.
21 Z. Sun, M. Yuan, L. Lin, H. Yang, H. Li, G. Sun, X. Yang and S. Ma, *Chem. Commun.*, 2019, **55**, 9729–9732.
22 P. Giannozzi, S. Baroni, N. Bonini, M. Calandra, R. Car, C. Cavazzoni, D. Ceresoli, G. L. Chiarotti, M. Cococcioni, I. Dabo, A. Dal Corso, S. de Gironcoli, S. Fabris, G. Fratesi, R. Gebauer, U. Gerstmann, C. Gougoussis, A. Kokalj, M. Lazzeri, L. Martin-Samos, N. Marzari, F. Mauri, R. Mazzarello, S. Paolini, A. Pasquarello, L. Paulatto, C. Sbraccia, S. Scandolo, G. Sclauzero, A. P. Seitsonen, A. Smogunov, P. Umari and R. M. Wentzcovitch, *J. Phys.: Condens. Matter*, 2009, **21**, 395502.
23 P. Giannozzi, O. Andreussi, T. Brumme, O. Bunau, M. Buongiorno Nardelli, M. Calandra, R. Car, C. Cavazzoni, D. Ceresoli, M. Cococcioni, N. Colonna, I. Carnimeo, A. Dal Corso, S. de Gironcoli, P. Delugas, R. A. DiStasio, A. Ferretti, A. Floris, G. Fratesi, G. Fugallo, R. Gebauer, U. Gerstmann, F. Giustino, T. Gorni, J. Jia, M. Kawamura, H. Y. Ko, A. Kokalj, E. Küçükbenli, M. Lazzeri, M. Marsili, N. Marzari, F. Mauri, N. L. Nguyen, H. V. Nguyen, A. Otero-de-la-Roza, L. Paulatto, S. Poncé, D. Rocca, R. Sabatini, B. Santra, M. Schlipf, A. P. Seitsonen, A. Smogunov, I. Timrov, T. Thonhauser, P. Umari, N. Vast, X. Wu and S. Baroni, *J. Phys.: Condens. Matter*, 2017, **29**, 465901.
24 P. Giannozzi, O. Baseggio, P. Bonfà, D. Brunato, R. Car, I. Carnimeo, C. Cavazzoni, S. de Gironcoli, P. Delugas, F. Ferrari Ruffino, A. Ferretti, N. Marzari, I. Timrov, A. Urru and S. Baroni, *J. Chem. Phys.*, 2020, **152**, 154105.
25 J. P. Perdew, K. Burke and M. Ernzerhof, *Phys. Rev. Lett.*, 1996, **77**, 3865–3868.
26 A. D. Becke, *Phys. Rev. A*, 1988, **38**, 3098–3100.
27 C. Lee, W. Yang and R. G. Parr, *Phys. Rev. B*, 1988, **37**, 785–789.
28 H. J. Monkhorst and J. D. Pack, *Phys. Rev. B*, 1976, **13**, 5188–5192.
29 Y. Peng, B. Lu, L. Chen, N. Wang, J. E. Lu, Y. Ping and S. Chen, *J. Mater. Chem. A*, 2017, **5**, 18261–18269.
30 X. Zhou, B. Wilfong, H. Vivanco, J. Paglione, C. M. Brown and E. E. Rodriguez, *J. Am. Chem. Soc.*, 2016, **138**, 16432–16442.
31 X. Han, K. Tao, D. Wang and L. Han, *Nanoscale*, 2018, **10**, 2735–2741.
32 B. Tian, W. Gao, X. Ning, Y. Wu and G. Lu, *Appl. Catal., B*, 2019, **249**, 138–146.
33 Y. Liu, Z. Min, J. Jiang, K. Sun, J. Gao, Y. Shang and B. Li, *ACS Sustainable Chem. Eng.*, 2019, **7**, 19442–19452.
34 L.-L. Feng, G.-D. Li, Y. Liu, Y. Wu, H. Chen, Y. Wang, Y.-C. Zou, D. Wang and X. Zou, *ACS Appl. Mater. Interfaces*, 2015, **7**, 980–988.
35 G. Eda, T. Fujita, H. Yamaguchi, D. Voiry, M. Chen and M. Chhowalla, *ACS Nano*, 2012, **6**, 7311–7317.
36 M. J. Thompson, K. J. Blakeney, S. D. Cady, M. D. Reichert, J. D. Pilar-Albaladejo, S. T. White and J. Vela, *Chem. Mater.*, 2016, **28**, 1668–1677.
37 D. Zeng, Y. Qiu, S. Peng, C. Chen, J. Zeng, S. Zhang and R. Xiao, *J. Mater. Chem. A*, 2018, **6**, 11306–11316.
38 G. Ma, X. Xu, Z. Feng, C. Hu, Y. Zhu, X. Yang, J. Yang and Y. Qian, *Nano Res.*, 2020, **13**, 802–809.
39 B. Tian, Z. Li, W. Zhen and G. Lu, *J. Phys. Chem. C*, 2016, **120**, 6409–6415.
40 V. Nicolosi, M. Chhowalla, M. G. Kanatzidis, M. S. Strano and J. N. Coleman, *Science*, 2013, **340**, 1226419.
41 J. Li, J. Wang, Y. Zhang, H. Wang, G. Lin, X. Xiong, W. Zhou, H. Luo and D. Li, *2D Materials*, 2018, **5**, 021001.
42 J. Meng, Z. Lan, T. Chen, Q. Lin, H. Liu, X. Wei, Y. Lu, J. Li and Z. Zhang, *J. Phys. Chem. C*, 2018, **122**, 24725–24731.
43 Y. Yang, H. Yao, Z. Yu, S. M. Islam, H. He, M. Yuan, Y. Yue, K. Xu, W. Hao, G. Sun, H. Li, S. Ma, P. Zapol and M. G. Kanatzidis, *J. Am. Chem. Soc.*, 2019, **141**, 10417–10430.
44 H. Wang, X.-B. Li, L. Gao, H.-L. Wu, J. Yang, L. Cai, T.-B. Ma, C.-H. Tung, L.-Z. Wu and G. Yu, *Angew. Chem., Int. Ed.*, 2018, **57**, 192–197.
45 H. Lin, N. Liu, Z. Shi, Y. Guo, Y. Tang and Q. Gao, *Adv. Funct. Mater.*, 2016, **26**, 5590–5598.
46 D.-Y. Wang, M. Gong, H.-L. Chou, C.-J. Pan, H.-A. Chen, Y. Wu, M.-C. Lin, M. Guan, J. Yang, C.-W. Chen, Y.-L. Wang, B.-J. Hwang, C.-C. Chen and H. Dai, *J. Am. Chem. Soc.*, 2015, **137**, 1587–1592.

47 Y. Wan, Z. Zhang, X. Xu, Z. Zhang, P. Li, X. Fang, K. Zhang, K. Yuan, K. Liu, G. Ran, Y. Li, Y. Ye and L. Dai, *Nano Energy*, 2018, **51**, 786–792.
48 H. Wang, Z. Lu, D. Kong, J. Sun, T. M. Hymel and Y. Cui, *ACS Nano*, 2014, **8**, 4940–4947.
49 X. Du, H. Su and X. Zhang, *ACS Sustainable Chem. Eng.*, 2019, **7**, 16917–16926.
50 J. Staszak-Jirkovský, C. D. Malliakas, P. P. Lopes, N. Danilovic, S. S. Kota, K.-C. Chang, B. Genorio, D. Strmcnik, V. R. Stamenkovic, M. G. Kanatzidis and N. M. Markovic, *Nat. Mater.*, 2016, **15**, 197–203.